International Journal of Engineering Science 85 (2014) 186–202

Contents lists available at ScienceDirect

International Journal of Engineering Science

journal homepage: www.elsevier.com/locate/ijengsci

Effect of the imperfect interface on the scattering of SH wave in a piezoelectric cylinder in a piezomagnetic matrix

Hsin-Yi Kuo *, Shu-Han Yu

Department of Civil Engineering, National Chiao Tung University, Hsinchu 30010, Taiwan

ARTICLE INFO

Article history:
Received 14 November 2013
Received in revised form 7 August 2014
Accepted 28 August 2014
Available online 7 October 2014

Keywords:
Multiferroic composite
Scattering
Anti-plane shear wave
Imperfect interface

ABSTRACT

We propose an exact analysis for the scattering of an anti-plane shear wave by a piezoelectric circular cylinder in a piezomagnetic matrix with imperfect interfaces. Two typical imperfect interfaces are investigated: mechanically stiff and highly electromagnetic conducting interfaces, and mechanically compliant and weakly electromagnetic conducting interfaces. We obtain the fields of scattered wave by means of series expansion, and show that whether the interface is a perfect contact or with imperfection, it is sufficient to invert a 4×4 matrix and an infinite number of 6×6 matrices to solve the involved unknowns. Numerical examples are presented to demonstrate the effect of the imperfection on the directivity patterns, scattering cross-sections, and potential field distributions. Results show that the mechanical or highly electric conducting imperfect interface has great effect on those values. Further, we observe a large low-frequency peak of the scattering cross-section for the composite with mechanical stiff imperfection.

© 2014 Elsevier Ltd. All rights reserved.

1. Introduction

Multiferroic composites consisting of piezoelectric and piezomagnetic phases exhibit a magneto-electric (ME) effect that is absent in each constituent. The ME effect, which is related to inducing an electric polarization by a magnetic field or conversely inducing a magnetization by an electric field, provides a variety of technological applications including magnetic field sensors, four-state memory cells, and energy harvesting devices, etc. This has motivated a number of experimental fabrications and theoretical predictions of ME composites. An extensive review of the literature and the state of the art can be found in Fiebig (2005), Nan, Bichurin, Dong, Viehland, and Srinivasan (2008), Bichurin, Petrov, Averkin, and Liverts (2010), Srinivasan (2010), Ma, Hu, Li, and Nan (2011).

The coupling in the multiferroic composite is achieved through the product property: the applied electric field creates a deformation in the piezoelectric phase which in turn induces a deformation in the piezomagnetic phase thereby inducing a magnetic field. The product ME effect is a new property determined by the mechanical interaction between the two phases. Therefore, the interface is critical in achieving the giant magnetoelectricity, and has also made the composites with imperfect interfaces the topic of a number of theoretical investigations. For example, Bichurin, Petrov, and Srinivasan (2003) introduced an interface coupling parameter that defines the degree to which the deformation of the piezoelectric layer follows that of the magnetostrictive layer. Nan, Liu, and Lin (2003) adopted the Green's function approach to study the interfacial bonding on the ME effect in the PZT-Terfenol-D laminated composite. Chang and Carman (2007) proposed a quasistatic

* Corresponding author.
E-mail address: hykuo@mail.nctu.edu.tw (H.-Y. Kuo).

http://dx.doi.org/10.1016/j.ijengsci.2014.08.006
0020-7225/© 2014 Elsevier Ltd. All rights reserved.

model including shear lag and demagnetization effect for predicting the ME effect in ME laminates. Wang, Pan, and Roy (2007) and Pan, Wang, and Wang (2009) employed the complex variable approach and Mori–Tanaka method to derive the effective moduli of ME fibrous composites with soft and stiff imperfect interfaces, respectively. Kuo (2013) generalized the classic work of Rayleigh (1892) in a periodic conductive perfect composite to the coupled magneto-electro-elastic fibrous composites with imperfect interfaces.

Recently, the dynamic behavior of ME composites has received considerable attention. For instance, Du, Shen, Ye, and Yue (2004) examined the scattering of anti-plane shear waves by a cylindrical inhomogeneity in a magneto-electro-elastic matrix with partial debonding. Chen and Shen (2007) extended the work of Levin, Michelitsch, and Gao (2002), who studied the elastic waves propagation in composites with piezoelectric fibers, to ME composites. They first solved the problem associated with a single cylindrical fiber, and then considered the problem associated with multiple fibers by employing the effective field approach. Soh and Liu (2006) studied the propagation of an interfacial shear horizontal (SH) wave in two bonded semi-infinite piezoelectric-piezomagnetic materials. Chen, Pan, and Chen (2007) presented an analytical treatment for the propagation of harmonic waves in magneto-electro-elastic multilayered plates. Liu, Fang, and Liu (2007) and Wang, Mai, and Niraula (2007) demonstrated the existence of a SH surface wave in a semi-infinite ME medium with hexagonal symmetry. Pang, Liu, Wang, and Zhao (2008) and Liu, Fang, Wei, and Zhao (2008) investigated the propagation of Rayleigh-type surface waves and Love waves in a piezoelectric-piezomagnetic layered half-space. Effects of the imperfect interface on the SH waves, interfacial SH waves, and reflection and transmission of planes waves in a multiferroic composites were also studied by Sun, Ju, Pan, and Li (2011), Huang, Li, and Lee (2009), and Pang and Liu (2011), respectively.

Motivated by these advances, and in a departure from previous works, this research is devoted to the anti-plane shear wave scattering by a piezoelectric circular cylinder of infinite length, which is imperfectly bonded to a piezomagnetic matrix. Both the fiber and matrix are assumed to be transversely isotropic, which are the materials frequently used in applications. Note that due to the polarization (magnetization) of the piezoelectric (piezomagnetic) material, the phase cannot possess the center of symmetry which makes the components of the piezoelectric (piezomagnetic) tensors be zero. Two kinds of imperfect interfaces are studied: (1) mechanically stiff and highly electromagnetic conducting interfaces, at which the potentials are continuous across the interface, while the normal component of flux undergoes a discontinuity which is proportional to the local surface Laplacian of the potential fields; and (2) mechanically compliant and weakly electromagnetic conducting interfaces, at which the normal flux are continuous, while the potentials are discontinuous at such contact. The jumps in potential components are further assumed to be proportional to their respective interface flux components.

The remainder of this paper is organized as follows. In Section 2 we formulate the governing equation for the anti-plane shear wave scattering by a piezoelectric circular cylinder in a piezomagnetic matrix. We obtain the solution in Section 3. Two kinds of imperfect contacts are studied: mechanically stiff and highly electromagnetic conducting interfaces, and mechanically compliant and weakly electromagnetic conducting interfaces. Numerical examples are demonstrated in Section 4 using composites of $BaTiO_3$ and $CoFe_2O_4$. We study the effect of the imperfection on the directivity pattern, scattering cross-section, and potential field distributions.

2. Formulation

Let us consider an unbounded piezomagnetic matrix containing an infinite long piezoelectric circular cylinder of radius a. Assume that each phase is transversely isotropic (i.e., has 6 mm symmetry) with the symmetry axes oriented with cylinders. We introduce a Cartesian coordinate system with x- and y-axes in the plane of the cross-section and z-axis along the axis of the cylinder. Assume that the cylinder is subjected to an incident anti-plane shear (SH) wave traveling in the positive x-direction.

The constitutive laws of the pth phase for the non-vanishing fields in a polar coordinate system can be recast in the compact form as (Wang, Pan et al., 2007)

$$\mathbf{\Sigma}_j^{(p)} = \mathbf{L}^{(p)}\mathbf{Z}_j^{(p)}, \quad j = r, \theta, \tag{2.1}$$

where for ease of the terminology, $p =$ "e" ($p =$ "m") refers to the piezoelectric (piezomagnetic) phase,

$$\mathbf{L}^{(e)} = \begin{pmatrix} C_{44} & e_{15} & 0 \\ e_{15} & -\kappa_{11} & 0 \\ 0 & 0 & -\mu_{11} \end{pmatrix}^{(e)}, \quad \mathbf{L}^{(m)} = \begin{pmatrix} C_{44} & 0 & q_{15} \\ 0 & -\kappa_{11} & 0 \\ q_{15} & 0 & -\mu_{11} \end{pmatrix}^{(m)},$$

$$\mathbf{\Sigma}_j^{(p)} = \begin{pmatrix} \sigma_{zj} \\ D_j \\ B_j \end{pmatrix}^{(p)}, \quad \mathbf{Z}_r^{(p)} = \frac{\partial \mathbf{\Phi}^{(p)}}{\partial r}, \quad \mathbf{Z}_\theta^{(p)} = \frac{\partial \mathbf{\Phi}^{(p)}}{r\partial \theta}, \quad \mathbf{\Phi}^{(p)} = \begin{pmatrix} w \\ \varphi \\ \psi \end{pmatrix}^{(p)}. \tag{2.2}$$

Here σ_{zj}, D_j, B_j are the stress, electric displacement, and magnetic flux. C_{44}, κ_{11}, and μ_{11} are, respectively, the elastic modulus, dielectric permittivity, and magnetic permeability, while e_{15} and q_{15} are the piezoelectric and piezomagnetic coefficients. w, φ, and ψ are the out-of-plane displacement, electric potential, and magnetic potential, respectively.

In the absence of body force, electric charge density and electric current density, the equilibrium equations are given by

$$\begin{pmatrix} C_{44} & e_{15} & q_{15} \\ e_{15} & -\kappa_{11} & 0 \\ q_{15} & 0 & -\mu_{11} \end{pmatrix}^{(p)} \begin{pmatrix} \nabla^2 w \\ \nabla^2 \varphi \\ \nabla^2 \psi \end{pmatrix}^{(p)} = \begin{pmatrix} -\rho\omega^2 w \\ 0 \\ 0 \end{pmatrix}^{(p)}, \tag{2.3}$$

where $\nabla^2 = \frac{1}{r}\frac{\partial}{\partial r} + \frac{\partial^2}{\partial r^2} + \frac{1}{r^2}\frac{\partial^2}{\partial \theta^2}$ represents the two-dimensional Laplace operator for the variable r and θ, and ρ is the mass density of the material. Note that throughout the paper, the time factor $e^{-i\omega t}$, where ω is the angular frequency, is suppressed. In addition, the quasi-static approximation for the electric and magnetic fields is used in the analysis. This is because the corresponding characteristic velocity of the electromagnetic waves has 10^5 times higher than that of the elastic waves. Therefore, we can neglect the electromagnetic field generated by the elastic field propagation (Levin et al., 2002).

To proceed, we introduce two new functions $\overline{\varphi}$ and $\overline{\psi}$ which are related to w, φ, and ψ by

$$\begin{aligned} \overline{\varphi}^{(e)} &= \varphi^{(e)} - \frac{e_{15}^{(e)}}{\kappa_{11}^{(e)}} w^{(e)}, \\ \overline{\psi}^{(m)} &= \psi^{(m)} - \frac{q_{15}^{(m)}}{\mu_{11}^{(m)}} w^{(m)}. \end{aligned} \tag{2.4}$$

Substitution of Eq. (2.4) into Eq. (2.1) yields the auxiliary constitutive laws:

$$\boldsymbol{\Sigma}_j^{(p)} = \overline{\mathbf{L}}^{(p)} \overline{\mathbf{Z}}_j^{(p)}, \tag{2.5}$$

$$\overline{\mathbf{Z}}_r^{(p)} = \frac{\partial \overline{\boldsymbol{\Phi}}^{(p)}}{\partial r}, \quad \overline{\mathbf{Z}}_\theta^{(p)} = \frac{\partial \overline{\boldsymbol{\Phi}}^{(p)}}{r\partial \theta},$$

where

$$\overline{\mathbf{L}}^{(e)} = \begin{pmatrix} \widetilde{C}_{44} & e_{15} & 0 \\ 0 & -\kappa_{11} & 0 \\ 0 & 0 & -\mu_{11} \end{pmatrix}^{(e)}, \quad \overline{\boldsymbol{\Phi}}^{(e)} = \begin{pmatrix} w \\ \overline{\varphi} \\ \psi \end{pmatrix}^{(e)} \tag{2.6}$$

for the piezoelectric material, and

$$\overline{\mathbf{L}}^{(m)} = \begin{pmatrix} \widetilde{C}_{44} & 0 & q_{15} \\ 0 & -\kappa_{11} & 0 \\ 0 & 0 & -\mu_{11} \end{pmatrix}^{(m)}, \quad \overline{\boldsymbol{\Phi}}^{(m)} = \begin{pmatrix} w \\ \varphi \\ \overline{\psi} \end{pmatrix}^{(m)} \tag{2.7}$$

for the piezomagnetic material. Further, the governing equation (2.3) decoupled into the Helmholtz and Laplace equations for the phase:

$$\begin{aligned} &(\nabla^2 + k_e^2) w^{(e)} = 0, \quad \nabla^2 \overline{\varphi}^{(e)} = 0, \quad \nabla^2 \psi^{(e)} = 0, \\ &(\nabla^2 + k_m^2) w^{(m)} = 0, \quad \nabla^2 \varphi^{(m)} = 0, \quad \nabla^2 \overline{\psi}^{(m)} = 0, \end{aligned} \tag{2.8}$$

where k is the wave number defined by

$$\begin{aligned} k_e^2 &\equiv \frac{\rho^{(e)}\omega^2}{\widetilde{C}_{44}^{(e)}}, \quad \widetilde{C}_{44}^{(e)} \equiv C_{44}^{(e)} + \frac{\left(e_{15}^{(e)}\right)^2}{\kappa_{11}^{(e)}}, \\ k_m^2 &\equiv \frac{\rho^{(m)}\omega^2}{\widetilde{C}_{44}^{(m)}}, \quad \widetilde{C}_{44}^{(m)} \equiv C_{44}^{(m)} + \frac{\left(q_{15}^{(m)}\right)^2}{\mu_{11}^{(m)}}, \end{aligned} \tag{2.9}$$

with $\widetilde{C}_{44}^{(p)}$ being the stiffened elastic constant.

3. Representation of the solution

Consider that the composite is subjected to an incident SH wave of unit amplitude propagating along the x-direction, and can be expanded as (Arfken & Weber, 2001)

$$e^{ik_m x} = J_0(k_m r) + 2\sum_{n=1}^{\infty} i^n J_n(k_m r)\cos n\theta, \tag{3.1}$$

where i is the imaginary number. The general solution to the Helmholtz and Laplace equations for the circular cylinder and its surrounding matrix can be expanded with respect to its center as

$$w^{(e)}(r,\theta) = A_0^w J_0(k_e r) + 2\sum_{n=1}^{\infty} i^n A_n^w J_n(k_e r)\cos n\theta,$$
$$\overline{\varphi}^{(e)}(r,\theta) = A_0^\varphi + \sum_{n=1}^{\infty} A_n^\varphi (r/a)^n \cos n\theta,$$
$$\psi^{(e)}(r,\theta) = A_0^\psi + \sum_{n=1}^{\infty} A_n^\psi (r/a)^n \cos n\theta \tag{3.2}$$

for the piezoelectric inclusion, and

$$w^{(m)}(r,\theta) = e^{ik_m x} + B_0^w H_0(k_m r) + 2\sum_{n=1}^{\infty} i^n B_n^w H_n(k_m r)\cos n\theta,$$
$$\varphi^{(m)}(r,\theta) = \sum_{n=1}^{\infty} B_n^\varphi (a/r)^n \cos n\theta,$$
$$\overline{\psi}^{(m)}(r,\theta) = \sum_{n=1}^{\infty} B_n^\psi (a/r)^n \cos n\theta \tag{3.3}$$

for the piezomagnetic matrix. Here (r,θ) is the polar coordinate centered at the origin of the inclusion. $J_n(\cdot)$ and $H_n(\cdot)$ are, respectively, the Bessel function of the first kind and the Hankel function of the first kind, both of order n. The coefficients $A_n^w, A_n^\varphi, A_n^\psi, B_n^w, B_n^\varphi, B_n^\psi$, are unknown constants to be determined from the interface and boundary conditions. The dimension of these coefficients are the same as the corresponding displacement w [L], electric potential [$ML^2A^{-1}T^{-3}$], and magnetic potential [A].

In order to treat the imperfect interface effect, we first resort to a more general three-phase composite of a similar distribution in which the inclusions possess a concentric elastic coating of thickness t and material parameter $\mathbf{L}_c = diag(C_{44}, -\kappa_{11}, -\mu_{11})$ (Hashin, 2001; Miloh & Benveniste, 1999; Torquato & Rintol, 1995.) By passing to the limit that $t \to 0$ and that either $\mathbf{L}_c^{-1} \to \mathbf{0}$ (mechanically stiff and highly electromagnetic conducting interfaces) or $\mathbf{L}_c \to \mathbf{0}$ (mechanically soft and weakly electromagnetic conducting interfaces), we recover the distribution of interest in which the interfacial property is characterized by the parameters $\boldsymbol{\alpha}$ and $\boldsymbol{\beta}$ given by:

$$\boldsymbol{\alpha} = \lim_{\substack{t\to 0 \\ \mathbf{L}_c^{-1}\to\mathbf{0}}} (t\mathbf{L}_c) = \begin{pmatrix} \alpha^w & 0 & 0 \\ 0 & \alpha^\varphi & 0 \\ 0 & 0 & \alpha^\psi \end{pmatrix} \tag{3.4}$$

for the mechanically stiff and highly electromagnetic conducting case, and

$$\boldsymbol{\beta} = \lim_{\substack{t\to 0 \\ \mathbf{L}_c\to\mathbf{0}}} \left(t\mathbf{L}_c^{-1}\right) = \begin{pmatrix} \beta^w & 0 & 0 \\ 0 & \beta^\varphi & 0 \\ 0 & 0 & \beta^\psi \end{pmatrix} \tag{3.5}$$

for the mechanically soft and weakly electromagnetic conducting case.

We first consider that the interface is mechanically stiff and highly electromagnetic conducting, that is,

$$\boldsymbol{\Sigma}_r^{(m)}\big|_{\partial V} - \boldsymbol{\Sigma}_r^{(e)}\big|_{\partial V} = \boldsymbol{\alpha}\Delta_s \boldsymbol{\Phi}^{(e)}\big|_{\partial V}, \quad \boldsymbol{\Phi}^{(m)}\big|_{\partial V} = \boldsymbol{\Phi}^{(e)}\big|_{\partial V}, \tag{3.6}$$

where $\Delta_s = \frac{1}{r^2}\frac{\partial^2}{\partial\theta^2}$ is the surface Laplace operator, and $\partial V : r = a$ denotes the interface between the matrix and the circular cylinder. The case where $\boldsymbol{\alpha} = \mathbf{0}$ corresponds to a perfect interface, whereas $\boldsymbol{\alpha}^{-1} = \mathbf{0}$ describes an isoexpansion and equipotential interface.

Using the orthogonality properties of trigonometric and Bessel (Hankel) functions, the interface conditions (3.6) provide

$$\mathbf{K}_0\mathbf{u}_0 = \mathbf{v}_0, \tag{3.7}$$

where

$$\mathbf{K}_0 = \begin{bmatrix} -H_0(k_m a) & J_0(k_e a) & 0 & 0 \\ 0 & \frac{e_{15}^{(e)}}{\kappa_{11}^{(e)}} J_0(k_e a) & 1 & 0 \\ -\frac{q_{15}^{(m)}}{\mu_{11}^{(m)}} H_0(k_m a) & 0 & 0 & 1 \\ -\widetilde{C}_{44}^{(m)} k_m H_0'(k_m a) & \widetilde{C}_{44}^{(e)} k_e J_0'(k_e a) & 0 & 0 \end{bmatrix},$$

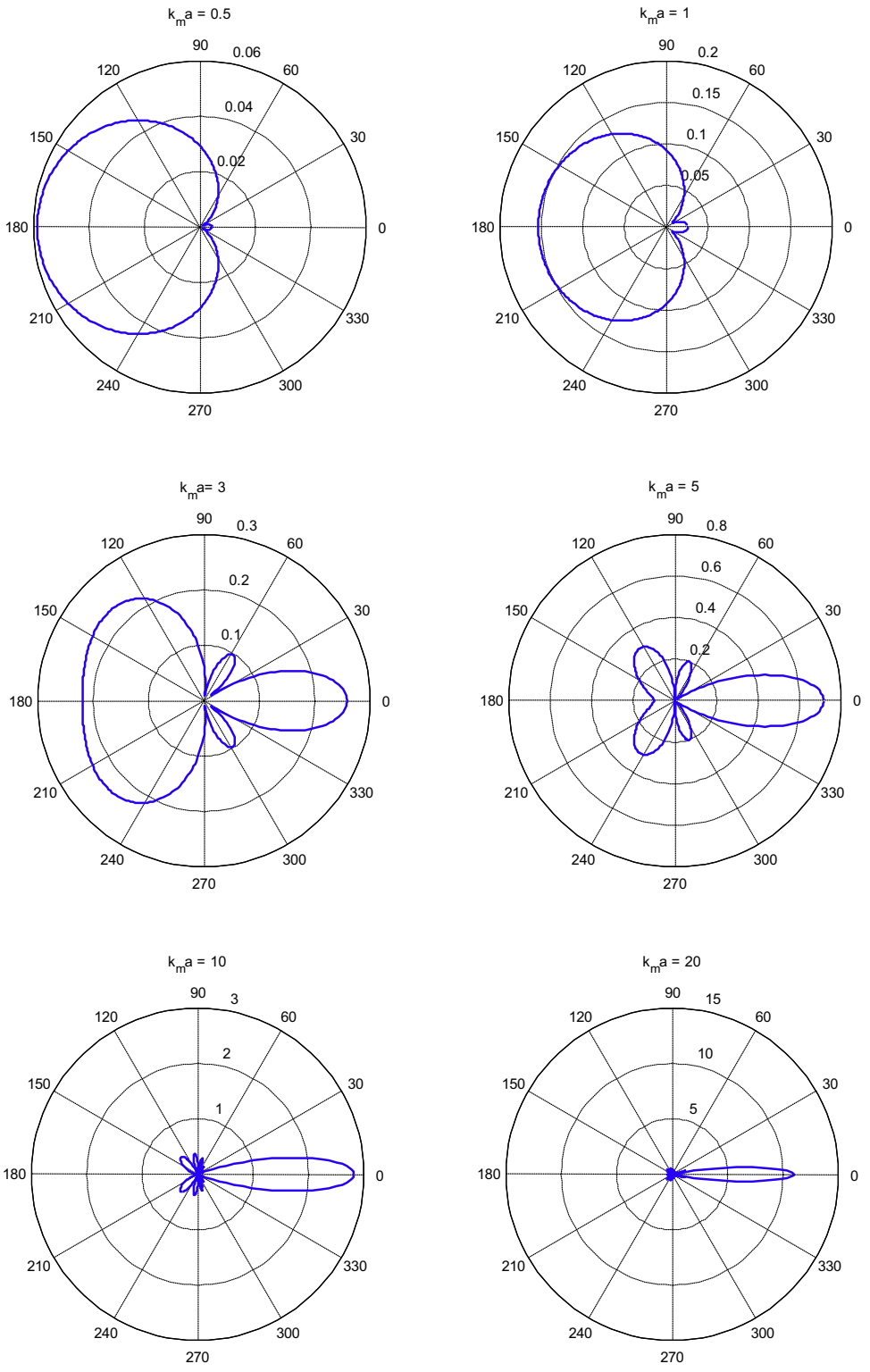

Fig. 1. Directivity patterns of the scattered wave for a cylinder with a perfect contact for various $k_m a$.

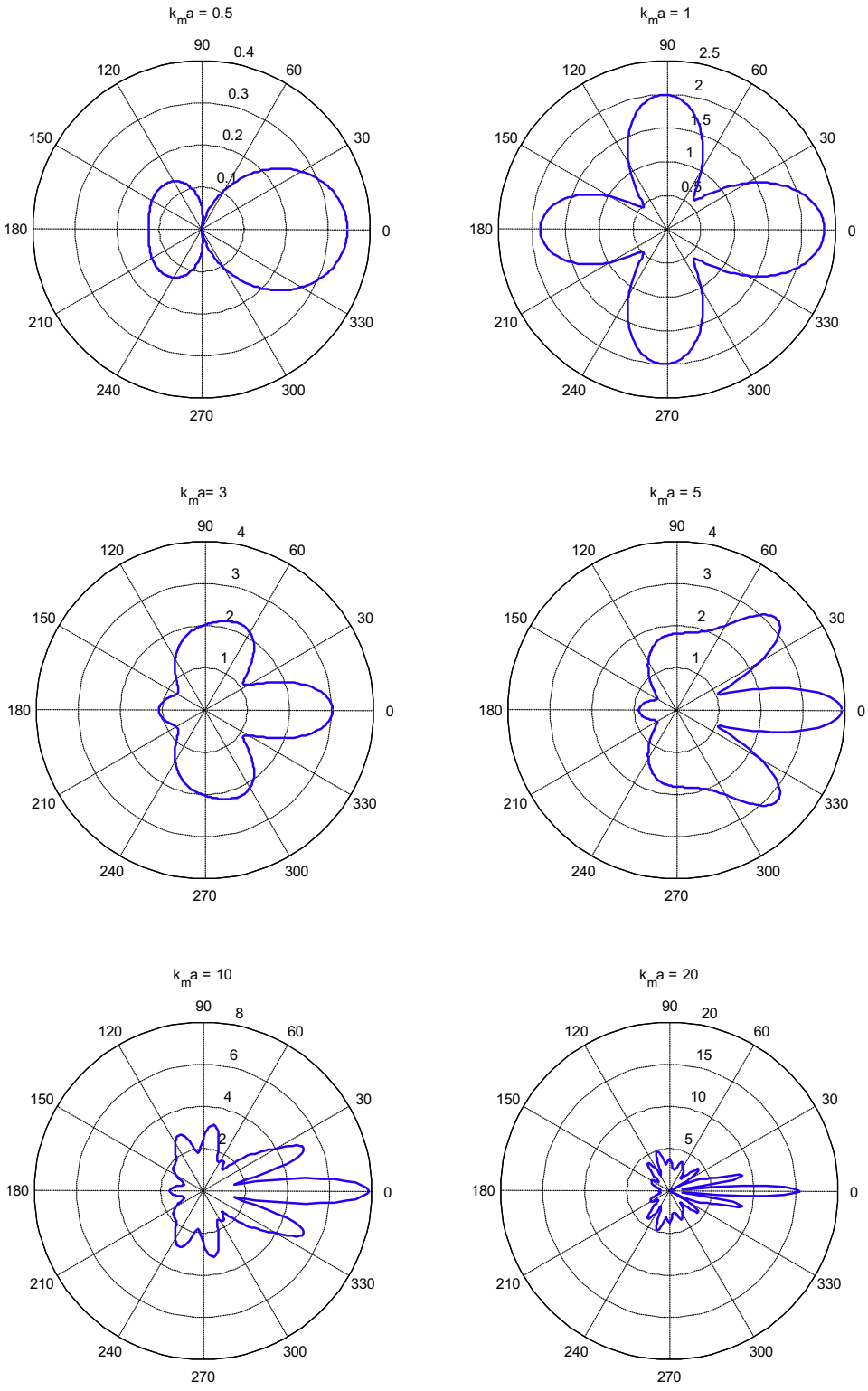

Fig. 2. Directivity patterns of the scattered wave for a cylinder with a stiff interface $\overline{\boldsymbol{\alpha}} = diag(1,0,0)$ for various $k_m a$.

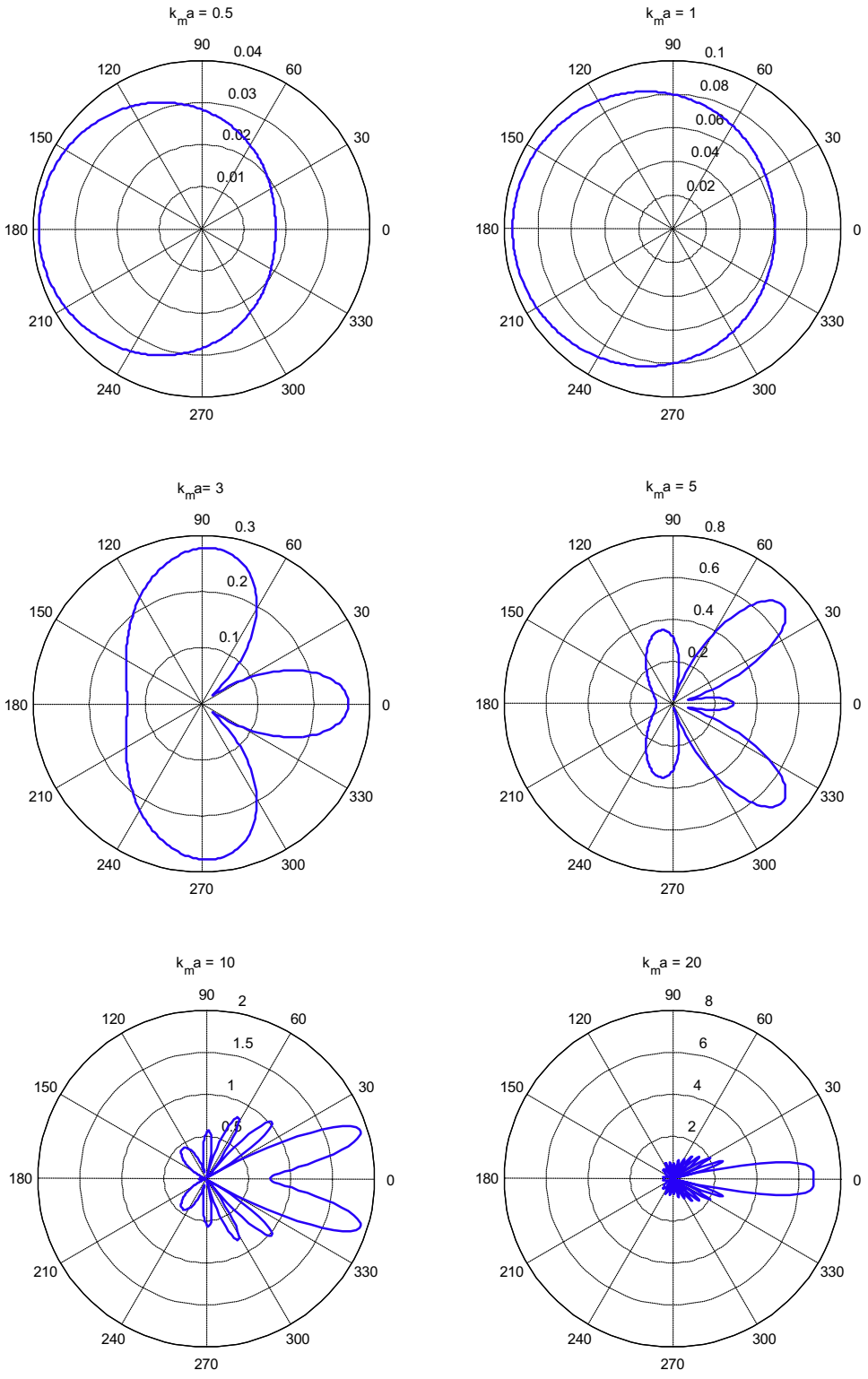

Fig. 3. Directivity patterns of the scattered wave for a cylinder with a highly electric conducting interface $\overline{\boldsymbol{\alpha}} = diag(0,1,0)$ for various $k_m a$.

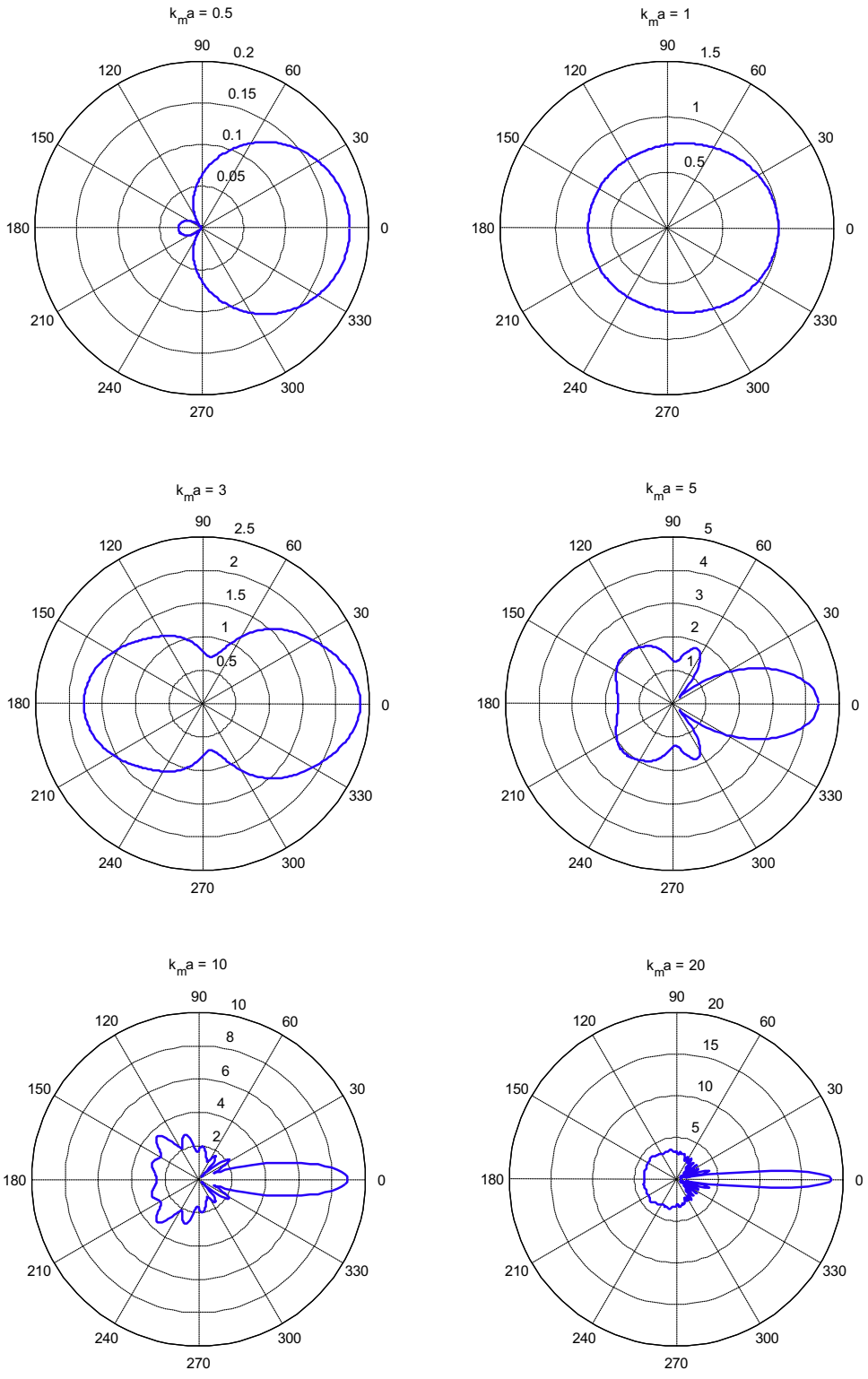

Fig. 4. Directivity patterns of the scattered wave for a cylinder with a soft interface $\overline{\boldsymbol{\beta}} = diag(1,0,0)$ for various $k_m a$.

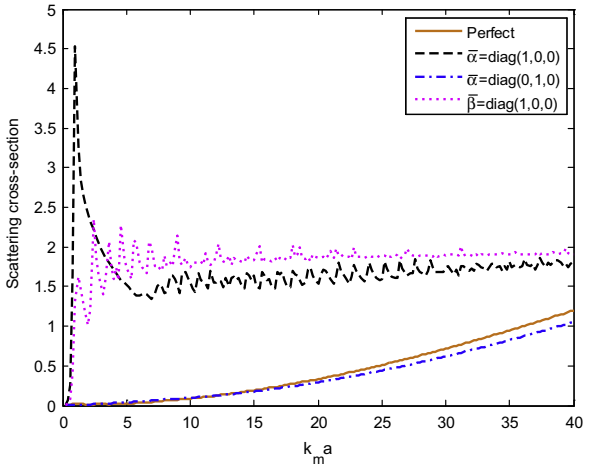

Fig. 5. Scattering cross-sections of the scattered shear wave for a perfect interface (solid line "-"), for a stiff interface (dashed line "- -"), for a highly electric conducting interface (dashed-dotted line "-·"), and for a compliant interface (dotted line "...").

$$\mathbf{u}_0 = \begin{pmatrix} B_0^w \\ A_0^w \\ A_0^\varphi \\ A_0^\psi \end{pmatrix}, \quad \mathbf{v}_0 = \begin{pmatrix} J_0(k_m a) \\ 0 \\ \frac{q_{15}^{(m)}}{\mu_{11}^{(m)}} J_0(k_m a) \\ \widetilde{C}_{44}^{(m)} k_m J_0'(k_m a) \end{pmatrix} \tag{3.8}$$

for $n = 0$, while

$$\mathbf{K}_n \mathbf{u}_n = \mathbf{v}_n, \tag{3.9}$$

$$\mathbf{K}_n = \begin{bmatrix} -2i^n H_n(k_m a) & 0 & 0 & 2i^n J_n(k_e a) & 0 & 0 \\ 0 & -1 & 0 & 2i^n \frac{e_{15}^{(e)}}{\kappa_{11}^{(e)}} J_n(k_e a) & 1 & 0 \\ -2i^n \frac{q_{15}^{(m)}}{\mu_{11}^{(m)}} H_n(k_m a) & 0 & -1 & 0 & 0 & 1 \\ -2i^n \widetilde{C}_{44}^{(m)} k_m H_n'(k_m a) & 0 & \frac{n q_{15}^{(m)}}{a} & \begin{matrix} 2i^n \widetilde{C}_{44}^{(e)} k_e J_n'(k_e a) \\ -2i^n \alpha^w \frac{n^2}{a^2} J_n(k_e a) \end{matrix} & \frac{n e_{15}^{(e)}}{a} & 0 \\ 0 & -\kappa_{11}^{(m)} & 0 & 2i^n \alpha^\varphi \frac{e_{15}^{(e)}}{\kappa_{11}^{(e)}} \frac{n}{a} J_n(k_e a) & \begin{matrix} \alpha^\varphi \frac{n}{a} \\ -\kappa_{11}^{(e)} \end{matrix} & 0 \\ 0 & 0 & \mu_{11}^{(m)} & 0 & 0 & \begin{matrix} \mu_{11}^{(e)} \\ -\alpha^\psi \frac{n}{a} \end{matrix} \end{bmatrix},$$

$$\mathbf{u}_n = \begin{pmatrix} B_n^w \\ B_n^\varphi \\ B_n^\psi \\ A_n^w \\ A_n^\varphi \\ A_n^\psi \end{pmatrix}, \quad \mathbf{v}_n = 2i^n \begin{pmatrix} J_n(k_m a) \\ 0 \\ \frac{q_{15}^{(m)}}{\mu_{11}^{(m)}} J_n(k_m a) \\ \widetilde{C}_{44}^{(m)} k_m J_n'(k_m a) \\ 0 \\ 0 \end{pmatrix} \tag{3.10}$$

for $n = 1, 2, 3, \ldots, \infty$. Here the prime $'$ denotes the derivative with respect to the variable in the parenthesis.

Next, we consider that the interface is mechanically soft and weakly electromagnetic conducting, i.e.,

$$\boldsymbol{\Sigma}_r^{(m)}\big|_{\partial V} = \boldsymbol{\Sigma}_r^{(e)}\big|_{\partial V}, \quad \boldsymbol{\Phi}^{(m)}\big|_{\partial V} - \boldsymbol{\Phi}^{(e)}\big|_{\partial V} = \boldsymbol{\beta}\boldsymbol{\Sigma}_r^{(e)}\big|_{\partial V}. \tag{3.11}$$

The case where $\boldsymbol{\beta} = 0$ corresponds to a perfect interface, whereas $\boldsymbol{\beta}^{-1} = \mathbf{0}$ describes a completely debonded and electric charge-free (insulating) interface. Analogous to the previous case, the interface conditions (3.11) give constraints (3.7) and (3.9), but with $\mathbf{K}_0$ and $\mathbf{K}_n$ replaced by

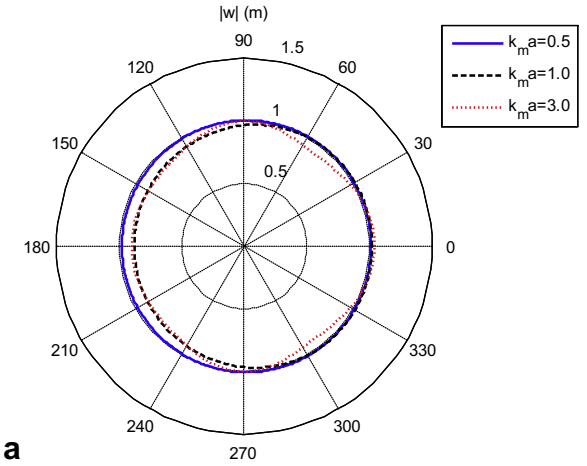

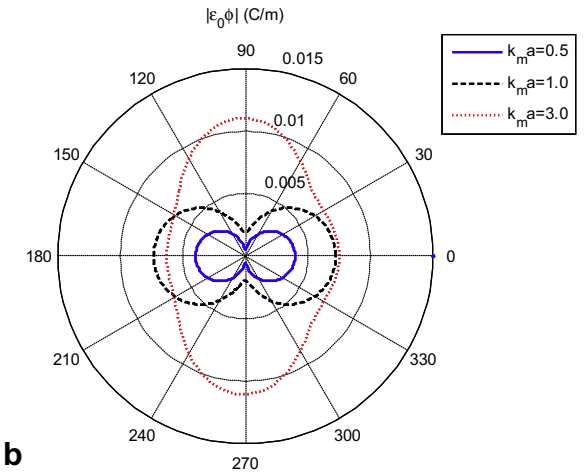

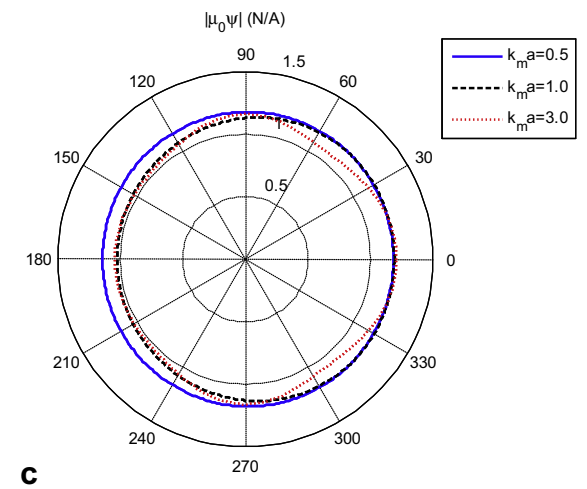

Fig. 6. Angular distribution of the absolute value of vertical displacement, electric potential and magnetic potential for a cylinder with a perfect contact versus θ for various $k_m a$.

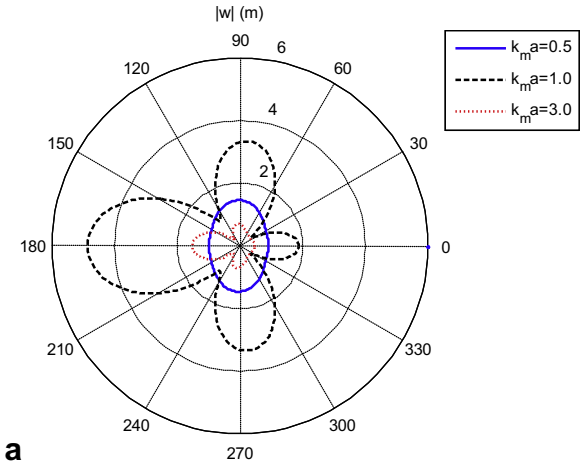

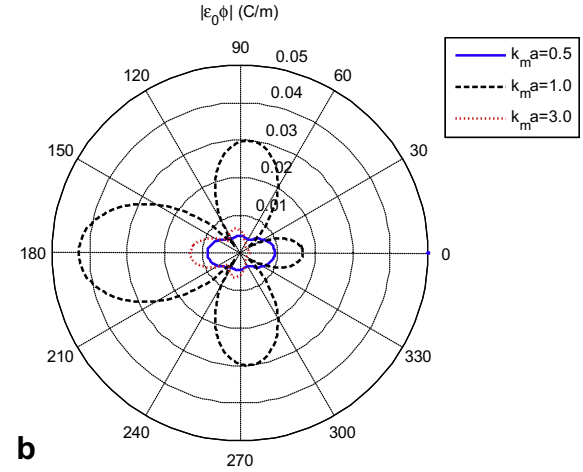

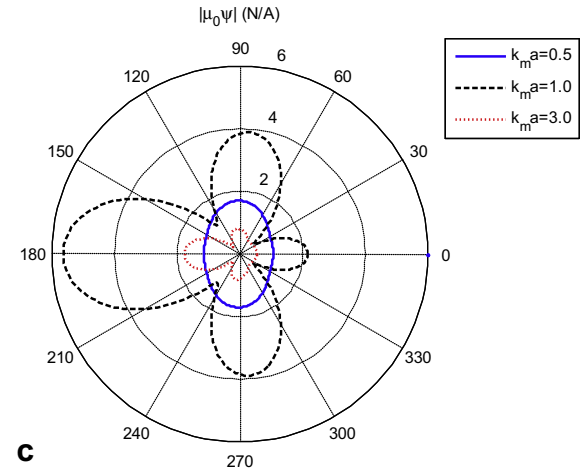

Fig. 7. Angular distribution of the absolute value of vertical displacement, electric potential and magnetic potential for a cylinder with a stiff interface $\overline{\boldsymbol{\alpha}} = diag(1,0,0)$ versus θ for various $k_m a$.

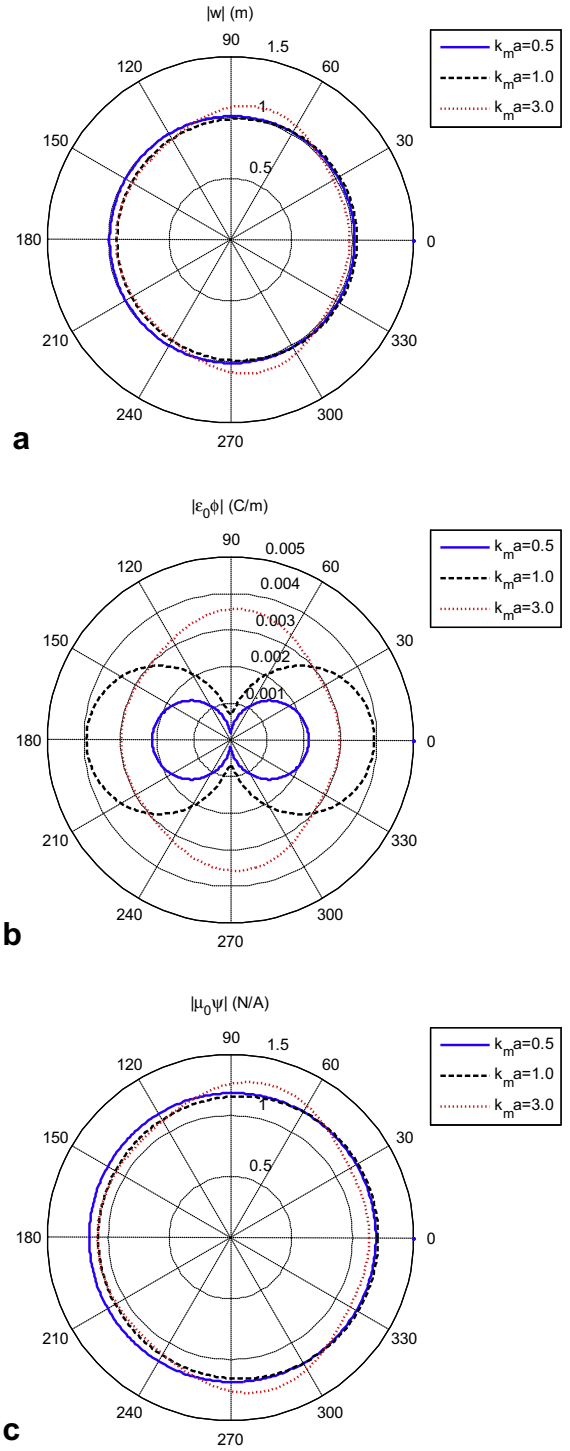

Fig. 8. Angular distribution of the absolute value of vertical displacement, electric potential and magnetic potential for a cylinder with a highly electric conducting interface $\overline{\boldsymbol{\alpha}} = diag(0, 1, 0)$ versus θ for various $k_m a$.

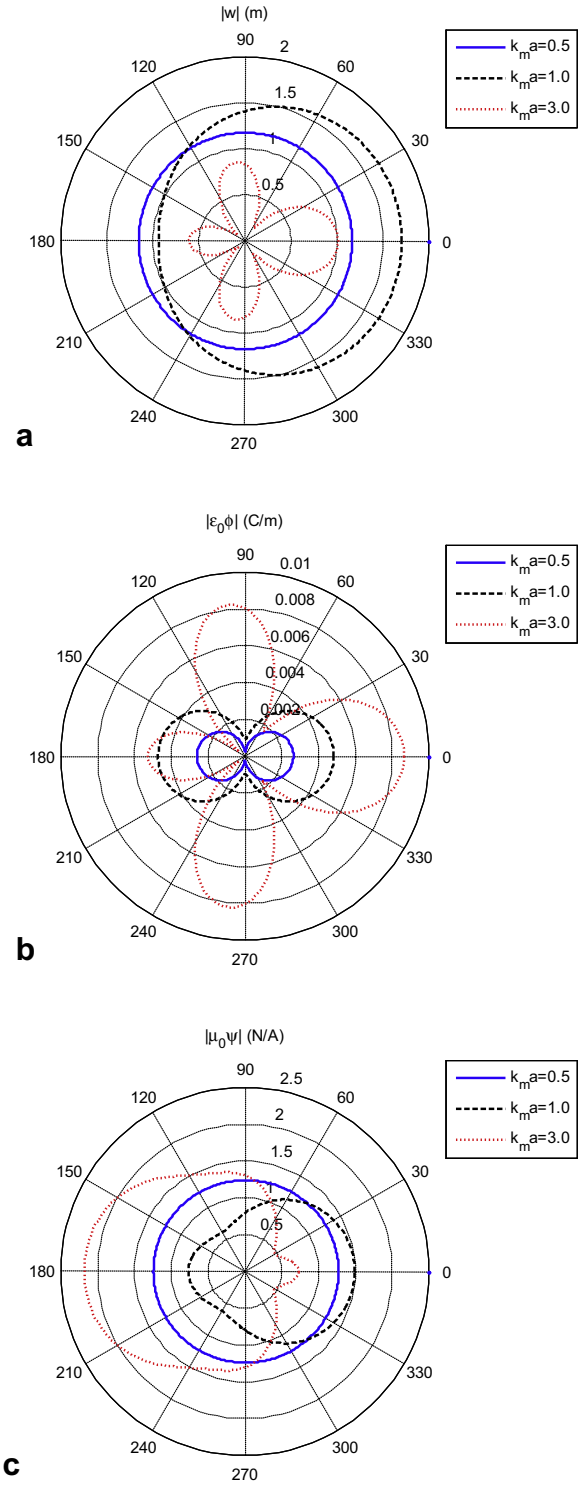

Fig. 9. Angular distribution of the absolute value of vertical displacement, electric potential and magnetic potential for a cylinder with a complaint interface $\overline{\boldsymbol{\beta}} = diag(1, 0, 0)$ versus θ for various $k_m a$.

$$\mathbf{K}_0 = \begin{bmatrix} -H_0(k_m a) & \beta^w \widetilde{C}_{44}^{(e)} k_e J_0'(k_e a) + J_0(k_e a) & 0 & 0 \\ 0 & \frac{e_{15}^{(e)}}{\kappa_{11}^{(e)}} J_0(k_e a) & 1 & 0 \\ -\frac{q_{15}^{(m)}}{\mu_{11}^{(m)}} H_0(k_m a) & 0 & 0 & 1 \\ -\widetilde{C}_{44}^{(m)} k_m H_0'(k_m a) & \widetilde{C}_{44}^{(e)} k_e J_0'(k_e a) & 0 & 0 \end{bmatrix}, \tag{3.12}$$

$$\mathbf{K}_n = \begin{bmatrix} -2i^n H_n(k_m a) & 0 & 0 & 2i^n \beta^w \widetilde{C}_{44}^{(e)} k_e J_n'(k_e a) + 2i^n J_n(k_e a) & \beta^w \frac{n e_{15}^{(e)}}{a} & 0 \\ 0 & -1 & 0 & 2i^n \frac{e_{15}^{(e)}}{\kappa_{11}^{(e)}} J_n(k_e a) & \beta^\varphi \frac{n\kappa_{11}^{(e)}}{a} + 1 & 0 \\ -2i^n \frac{q_{15}^{(m)}}{\mu_{11}^{(m)}} H_n(k_m a) & 0 & -1 & 0 & 0 & \beta^\psi \frac{n\mu_{11}^{(e)}}{a} + 1 \\ -2i^n \widetilde{C}_{44}^{(m)} k_m H_n'(k_m a) & 0 & \frac{n q_{15}^{(m)}}{a} & 2i^n \widetilde{C}_{44}^{(e)} k_e J_n'(k_e a) & \frac{n e_{15}^{(e)}}{a} & 0 \\ 0 & -\kappa_{11}^{(m)} & 0 & 0 & -\kappa_{11}^{(e)} & 0 \\ 0 & 0 & \mu_{11}^{(m)} & 0 & 0 & \mu_{11}^{(e)} \end{bmatrix}. \tag{3.13}$$

4. Numerical results and discussion

As a numerical example, we apply our solution to the $BaTiO_3$ (BTO, piezoelectric)-$CoFe_2O_4$ (CFO, piezomagnetic) multiferroic composite. Both of them are transversely isotropic. The independent material constants of BTO are $C_{44} = 43 \times 10^9$ N/m^2, $e_{15} = 11.6$ C/m^2, $\kappa_{11} = 11.2 \times 10^{-9}$ C^2/Nm^2, $\mu_{11} = 5 \times 10^{-6}$ Ns^2/C^2, $\rho = 6.02 \times 10^3$ kg/m^3, while those of CFO are $C_{44} = 45.3 \times 10^9$ N/m^2, $q_{15} = 550$ N/Am, $\kappa_{11} = 0.08 \times 10^{-9}$ C^2/Nm^2, $\mu_{11} = 590 \times 10^{-6}$ Ns^2/C^2, $\rho = 5.20 \times 10^3$ kg/m^3 (Cannas, Falqui, Musinu, Peddis, & Piccaluga, 2006; Wang, Pan et al., 2007). Here the xy plane is an isotropic plane and the poling direction/magnetic axis is along the z-direction. Further, the following dimensionless imperfect parameters have been chosen for computation in the analysis: $\overline{\alpha^w} = \alpha^w/(C_{44}^{(e)} a)$, $\overline{\alpha^\varphi} = -\alpha^\varphi/(\kappa_{11}^{(e)} a)$, $\overline{\alpha^\psi} = -\alpha^\psi/(\mu_{11}^{(e)} a)$, $\overline{\beta^w} = \beta^w C_{44}^{(e)}/a$, $\overline{\beta^\varphi} = -\beta^\varphi \kappa_{11}^{(e)}/a$, and $\overline{\beta^\psi} = -\beta^\psi \mu_{11}^{(e)}/a$.

In our calculation, the series in Eqs. (3.2) and (3.3) are truncated at $n = N$ with a relative error less than 1%. It is observed that N is a monotonically increasing function of the normalized frequency $k_m a$. That is, the smaller truncated number of N can be adopted when the wave frequency is smaller.

4.1. Directivity pattern

The directivity patterns of the scattered waves are of interest in practical applications. The scattered component in the mechanical displacement $w^{(m)}$ in the far field has the following asymptotic behavior (Abramowitz & Stegun, 1972; Wang, Pan et al., 2007)

$$w_s^{(m)} = \sqrt{\frac{2}{\pi k_m r}} e^{i\left(k_m r - \frac{\pi}{4}\right)} \left[B_0^w + 2\sum_{n=1}^{\infty} i^n B_n^w e^{-\frac{in\pi}{2}} \cos(n\theta) \right], \quad r \to \infty, \tag{4.1}$$

where the subscript s denotes the scattering field in the matrix.

Substituting (4.1) into $(3.3)_{2,3}$ and $(2.4)_2$, the stress $\sigma_{zr,s}^{(m)}$, electric potential $\varphi_s^{(m)}$ and magnetic potential $\psi_s^{(m)}$ in the far field induced by the scattered shear wave are given by

$$\sigma_{zr,s}^{(m)} = ik_m \widetilde{C}_{44}^{(m)} w_s^{(m)}, \quad \varphi_s^{(m)} = 0, \quad \psi_s^{(m)} = \frac{q_{15}^{(m)}}{\mu_{11}^{(m)}} w_s^{(m)}, \quad r \to \infty. \tag{4.2}$$

Therefore, the far field behaviors of the stress, mechanical displacement, and magnetic potential in the piezomagnetic matrix at the far field are related. The far field directivity pattern of the scattered shear wave is defined by Liu, Wu, and Ying (2000)

$$D(\theta) = \left| B_0^w + 2\sum_{n=1}^{\infty} i^n B_n^w e^{-\frac{in\pi}{2}} \cos(n\theta) \right|, \tag{4.3}$$

which exhibits the angular distribution of the absolute value of the amplitude of the stress component $\sigma_{zr}^{(m)}$ at a large distance from the cylinder.

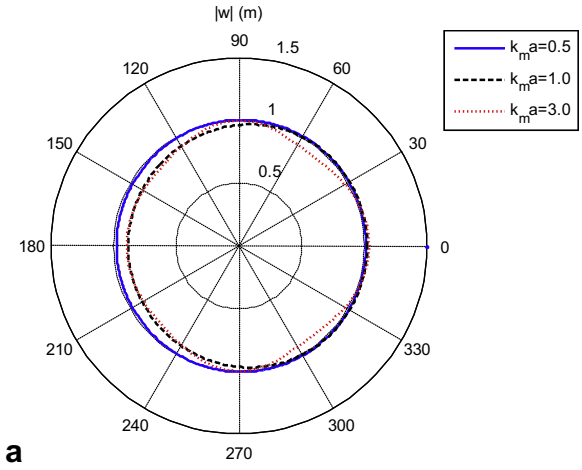

a

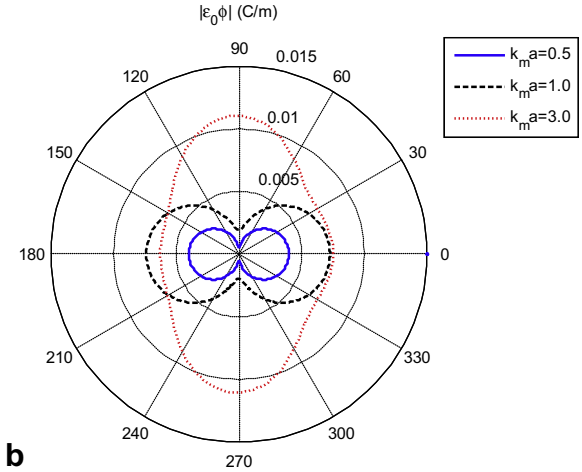

b

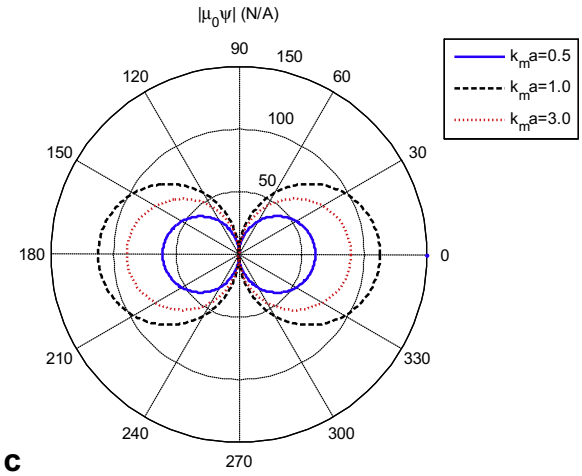

c

Fig. 10. Angular distribution of the absolute value of vertical displacement, electric potential and magnetic potential for a cylinder with a weakly magnetic conducting interface $\overline{\boldsymbol{\beta}} = diag(0, 0, 1)$ versus θ for various $k_m a$.

Fig. 1 shows the directivity patterns of the scattered waves for a perfectly bonded cylinder ($\overline{\boldsymbol{\alpha}} = \mathbf{0}, \overline{\boldsymbol{\beta}} = \mathbf{0}$) under six different frequencies $k_m a = 0.5, 1, 3, 5, 10, 20$. Figs. 2 and 3 represent, respectively, the corresponding results for a stiff interface with $\overline{\boldsymbol{\alpha}} = diag(1,0,0)$ and those for a highly electric conducting interface with $\overline{\boldsymbol{\alpha}} = diag(0,1,0)$. Fig. 4 plots the results for a compliant interface with $\overline{\boldsymbol{\beta}} = diag(1,0,0)$. We do not show the plots for a highly magnetic conducting interface ($\overline{\boldsymbol{\alpha}} = diag(0,0,1)$), and the weakly electromagnetic conducting interface ($\overline{\boldsymbol{\beta}} = diag(0,1,0), \overline{\boldsymbol{\beta}} = diag(0,0,1)$) since we observe that there are only minor effect of $\alpha^{\psi}, \beta^{\varphi}$, and β^{ψ} on the directivity pattern.

From these figures, we observe that for the mechanical imperfection interface (Figs. 2 and 4), the directivity pattern becomes complicated and concentrated at $\theta = 0$ as the frequency increases, which means that the directivity pattern of the shadow side ($\theta = 0$) of the piezoelectric cylinder is more sensitive than that of the incident side ($\theta = \pi$). However, for the perfect interface as shown in Fig. 1, the maximum of the directivity pattern occurs at the incident side at low frequency, while the pattern becomes complicated and concentrated along the opposite of the incident wave direction at high wavenumbers. For the highly electric conducting interface (Fig. 3), the maximum of the directivity pattern first occurs at the incident side at low frequency. As the frequency increases, the maximum of the pattern occurs symmetrically with respect to the x-axis and eventually merged along $\theta = 0$. All the above imperfections significantly alter both the shape and size of the directivity pattern, and these multiple peaks results from the interference caused by the incident and reflected waves.

4.2. Scattering cross-section

The scattering cross-section of the shear wave for the cylinder is the ratio of the total energy flow carried outwards by the scattered wave to the energy flow of the incident wave through a normal area that is equal to the cross-section area of the scatterer, which is defined by Liu et al., 2000

$$Q = \frac{2\left|B_0^w\right|^2 + 2\sum_{n=1}^{\infty}\left|i^n B_n^w\right|^2}{k_m a}. \tag{4.4}$$

Fig. 5 is the scattering cross-section of the scattered shear wave for a perfect interface (solid line "-"), for a stiff interface (dashed line "- -"), for a highly electric conducting interface (dashed-dotted line "-·"), and for a compliant interface (dotted line "…"). For the other imperfect parameters, they have the same results for that of the perfect contact case. The curves are calculated in steps of $k_m a = 0.1$ and $N = 60$. The frequency range is $k_m a = 0$ to 40. The most striking feature of the scattering cross-section curves is the existence of a sequence of maximum and minimum for the scattered shear wave when the interface is a mechanical imperfect contact. Further, a large low-frequency peak occurring at $k_m a = 1$, which corresponds to the resonance scattering, can appear for a mechanically stiff imperfect interface with $\overline{\boldsymbol{\alpha}} = diag(1,0,0)$. We will see how this effect influence the field distribution in the following subsection. We further remark that except there exists small fluctuation at small frequency, the scattering cross-section for a perfect contact and remaining kinds of interface imperfection is in general a monotonically increasing function of the normalized frequency $k_m a$.

4.3. Mechanical displacement, electric potential, and magnetic potential

Fig. 6 is the angular distribution of vertical displacement, electric potential and magnetic potential for a cylinder with a perfect contact versus θ for various $k_m a$. Figs. 7–10 show the corresponding plots for a stiff interface with $\overline{\boldsymbol{\alpha}} = diag(1,0,0)$ (Fig. 7), for a highly electric conducting interface with $\overline{\boldsymbol{\alpha}} = diag(0,1,0)$ (Fig. 8), for a compliant interface with $\overline{\boldsymbol{\beta}} = diag(1,0,0)$ (Fig. 9), and for a weakly magnetic conducting interface with $\overline{\boldsymbol{\beta}} = diag(0,0,1)$ (Fig. 10). Similarly we do not show the figures for a highly magnetic conducting interface ($\overline{\boldsymbol{\alpha}} = diag(0,0,1)$), and for a weakly electric conducting interface ($\overline{\boldsymbol{\beta}} = diag(0,1,0)$) since we observe that there are only minor effect of α^{ψ} and β^{φ} on the potential distribution.

From Figs. 6(a)–10(a) and 6(c)–9(c), we observe that at $k_m a = 0.5$, the distributions of displacement $|w|$ and magnetic potential $|\mu_0 \psi|$ around the cylinder are almost uniform except those with the mechanical stiff imperfect interface (Fig. 7). In addition, multiple peaks and larger value appear along the circumference of the piezoelectric cylinder at $k_m a = 1$ in Fig. 7, which correspond to the resonance scattering shown in Fig. 5. Further, we observe that the distributions of the electric potential $|\varepsilon_0 \varphi|$ are different from those of the displacement and magnetic potential. Each distribution has two lobes and is symmetric with respect to both x- and y- axes at $k_m a = 0.5$ and 1.0 (Figs. 6(b), 8(b)–10(b)). Finally, it is observed the magnetic potential is extremely large for a cylinder with a weakly magnetic conducting interface (Fig. 10(c)), although the other two potentials are the same as those of the perfect case.

5. Concluding remarks

In summary, we have presented an exact analysis to the anti-plane shear wave scattering by a piezoelectric fiber in a piezomagnetic matrix with imperfect interfaces. Both mechanically stiff and highly electromagnetic conducting interfaces, and mechanically soft and weakly electromagnetic conducting interfaces are considered. Our analyses show that whether the interface is a perfect contact or with imperfection, it is sufficient to invert a 4×4 matrix and an infinite number of

6×6 matrices to solve the involved unknowns. Comparing with the results of the perfect contact case, the mechanical imperfection or highly electric conducting imperfect interface has great influence on the value and distribution of the directivity pattern, scattering cross-section, mechanical displacement, and electromagnetic potential, while the weakly magnetic conducting interface has only influence on the value and distribution of the magnetic potential. The other imperfect parameters, i.e., the highly (weakly) magnetic (electric) conducting imperfection has really minor effect on these figures of merits. We also observe a large low-frequency peak of the scattering cross-sections with mechanical stiff imperfection, and a sequence of small high-frequency peak for that with mechanical compliant imperfection. We note that for clarity we show the case of a piezoelectric fiber in a piezomagnetic matrix in the paper. However, based on this framework, it can be easily extended to its complimentary counterpart of a piezomagnetic fiber in a piezoelectric matrix, and can also be easily extended to take into account different kinds of imperfect interface conditions. The present theoretical framework provides a general guideline for the bonding interface of the piezoelectric and piezomagnetic phases under dynamic loading. Further, while in the present scattering problem, only a single piezoelectric cylinder is considered, the corresponding wave scattering by a cluster of piezoelectric cylinders is also of interest and forms the subject of future study.

Acknowledgment

We are pleased to thank Prof. Chih-Yu Kuo at the Academia Sinica, Taiwan, for helpful discussion. We also gratefully acknowledges the support of the National Science Council, Taiwan, through Grant NSC 102-2221-E-009-087.

References

Abramowitz, M., & Stegun, I. A. (1972). *Handbook of mathematical functions with formulas, graphs, and mathematical tables*. New York: Dover.
Arfken, G. B., & Weber, H. J. (2001). *Mathematical methods for physicists*. San Diego: Academic Press.
Bichurin, M. I., Petrov, V. M., & Srinivasan, G. (2003). Theory of low-frequency magnetoelectric coupling in magnetostrictive-piezoelectric bilayers. *Physical Review B, 68*, 054402.
Bichurin, M. I., Petrov, V. M., Averkin, S. V., & Liverts, E. (2010). Present status of theoretical modeling the magnetoelectric effect in magnetostrictive-piezoelectric nanostructures. Part I: Low frequency and electromechanical resonance ranges. *Journal of Applied Physics, 107*, 053904.
Cannas, C., Falqui, A., Musinu, A., Peddis, D., & Piccaluga, G. (2006). $CoFe_2O_4$ nanocrystalline powders prepared by citrate-gel methods: Synthesis, structure and magnetic properties. *Journal of Nanoparticle Research, 8*, 255–267.
Chang, C.-M., & Carman, G. P. (2007). Modeling shear lag and demagnetization effects in magneto-electric laminate composites. *Physical Review B, 76*, 134116.
Chen, P., & Shen, Y. (2007). Propagation of axial shear magneto-electro-elastic waves in piezoelectric-piezomagnetic composites with randomly distributed cylindrical inhomogeneities. *International Journal of Solids and Structures, 44*, 1511–1532.
Chen, J., Pan, E., & Chen, H. (2007). Wave propagation in magneto-electro-elastic multilayered plates. *International Journal of Solids and Structures, 44*, 1073–1085.
Du, J. K., Shen, Y. P., Ye, D. Y., & Yue, F. R. (2004). Scattering of anti-plane shear waves at a partially debonded magneto-electro-elastic circular cylindrical inhomogeneity. *International Journal of Engineering Science, 42*, 887–913.
Fiebig, M. (2005). Revival of the magnetoelectric effect. *Journal of Physics D: Applied Physics, 38*, R123–R152.
Hashin, Z. (2001). Thin interphase/imperfect interface in conduction. *Journal of Applied Physics, 89*, 2261–2267.
Huang, Y., Li, X.-F., & Lee, K. Y. (2009). Interfacial shear horizontal (SH) waves propagating in a two-phase piezoelectric/piezomagnetic structure with an imperfect interface. *Philosophical Magazine Letters, 89*, 95–103.
Kuo, H.-Y. (2013). Effective property of multiferroic composites with imperfect interfaces. *Smart Materials and Structures, 22*, 105005.
Levin, V. M., Michelitsch, T. M., & Gao, H. (2002). Propagation of electroacoustic waves in the transversely isotropic piezoelectric medium reinforced by randomly distributed cylindrical inhomogeneities. *International Journal of Solids and Structures, 39*, 5013–5051.
Liu, J., Fang, D., & Liu, X. (2007). A shear horizontal surface wave in magnetoelectric materials. *IEEE Transactions on Ultrasonics Ferroelectrics and Frequency Control, 54*, 1287–1289.
Liu, J.-X., Fang, D.-N., Wei, W.-Y., & Zhao, X.-F. (2008). Love waves in layered piezoelectric/piezomagnetic structures. *Journal of Sound and Vibration, 315*, 146–156.
Liu, Y., Wu, R.-S., & Ying, C. F. (2000). Scattering of elastic waves by an elastic or viscoelastic cylinder. *Geophysical Journal International, 142*, 439–460.
Ma, J. M., Hu, J., Li, Z., & Nan, C.-W. (2011). Recent progress in multiferroic magnetoelectric composites: From bulk to thin films. *Advanced Materials, 23*, 1062–1087.
Miloh, T., & Benveniste, Y. (1999). On the effective conductivity of composites with ellipsoidal inhomogeneities and highly conducting interfaces. *Proceedings of the Royal Society A, 455*, 2687–2706.
Nan, C.-W., Liu, G., & Lin, Y. (2003). Influence of interfacial bonding on giant magnetoelectric response of multiferroic laminated composites of $Tb_{1-x}Dy_xFe_2$ and $PbZr_xTi_{1-x}O_3$. *Applied Physics Letters, 83*, 4366–4368.
Nan, C.-W., Bichurin, M. I., Dong, S., Viehland, D., & Srinivasan, G. (2008). Multiferroic magnetoelectric composites: Historical perspective, status, and future directions. *Journal of Applied Physics, 103*, 031101.
Pan, E., Wang, X., & Wang, R. (2009). Enhancement of magnetoelectric effect in multiferroic fibrous nancomposites via size-dependent material properties. *Applied Physics Letters, 95*, 181904.
Pang, Y., & Liu, J.-X. (2011). Reflection and transmission of plane waves at an imperfectly bonded interface between piezoelectric and piezomagnetic media. *European Journal of Mechanics A/Solids, 30*, 731–740.
Pang, Y., Liu, J.-X., Wang, Y.-S., & Zhao, X.-F. (2008). Propagation of Rayleigh-type surface waves in a transversely isotropic piezoelectric layer on a piezomagnetic half-space. *Journal of Applied Physics, 103*, 074901.
Rayleigh, L. (1892). On the influence of obstacles arranged in rectangular order upon the properties of a medium. *Philosophical Magazine, 34*, 481–502.
Soh, A. K., & Liu, J. X. (2006). Interfacial shear horizontal waves in a piezoelectric-pieozmagnetic bi-material. *Philosophical Magazine Letters, 86*, 31–35.
Srinivasan, G. (2010). Magnetoelectric composites. *Annual Review of Materials Research, 40*, 153–178.
Sun, W.-H., Ju, G.-L., Pan, J.-W., & Li, Y.-D. (2011). Effects of the imperfect interface and piezoelectric/piezomagnetic stiffening on the SH wave in a multiferroic composite. *Ultrasonics, 51*, 831–838.
Torquato, S., & Rintoul, M. D. (1995). Effect of the interface on the properties of composite media. *Physical Review Letters, 75*, 4067–4070.
Wang, B. L., Mai, Y.-W., & Niraula, O. P. (2007). A horizontal shear surface wave in magnetoelectroelastic materials. *Philosophical Magazine Letters, 87*, 53–58.
Wang, X., Pan, E., & Roy, A. K. (2007). Scattering of antiplane shear wave by a piezoelectric circular cylinder with an imperfect interface. *Acta Mechanica, 193*, 177–195.